PCCP

ROYAL SOCIETY OF CHEMISTRY

PAPER

View Article Online
View Journal | View Issue

Cite this: *Phys. Chem. Chem. Phys.*, 2020, **22**, 15354

First-principles investigation of nonmetal doped single-layer BiOBr as a potential photocatalyst with a low recombination rate†

Mohammed M. Obeid, *[a] C. Stampfl, [b] A. Bafekry, [cd] Z. Guan, [e] H. R. Jappor, [f] C. V. Nguyen, [g] M. Naseri, [h] D. M. Hoat, [i] N. N. Hieu, [jk] A. E. Krauklis, [l] Tuan V. Vu [m] and D. Gogova [n]

Nonmetal doping is an effective approach to modify the electronic band structure and enhance the photocatalytic performance of bismuth oxyhalides. Using density functional theory, we systematically examine the fundamental properties of single-layer BiOBr doped with boron (B) and phosphorus (P) atoms. The stability of the doped models is investigated based on the formation energies, where the substitutional doping is found to be energetically more stable under O-rich conditions than under Bi-rich ones. The results showed that substitutional doping of P atoms reduced the bandgap of pristine BiOBr to a greater extent than that of boron substitution. The calculation of the effective masses reveals that B doping can render the electrons and holes of pristine BiOBr lighter and heavier, respectively, resulting in a slower recombination rate of photoexcited electron–hole pairs. Based on the results of HOMO–LUMO calculations, the introduction of B atoms tends to increase the number of photocatalytically active sites. The top of the valence band and the conduction band bottom of the B doped BiOBr monolayer match well with the water redox potentials in an acidic environment. The absorption spectra propose that B(P) doping causes a red-shift. Overall, the results predict that nonmetal-doped BiOBr monolayers have a reduced bandgap, a slow recombination rate, more catalytically active sites, enhanced optical absorption edges, and reduced work functions, which will contribute to superior photocatalytic performance.

Received 14th April 2020,
Accepted 16th June 2020

DOI: 10.1039/d0cp02007a

rsc.li/pccp

1. Introduction

Semiconductor photocatalysts have attracted wide research interest thanks to their prospective application in removing inorganic/organic impurities and splitting water. Although conventional TiO_2 has been confirmed to be an outstanding photocatalyst, its wide bandgap (3.2 eV) offers no visible light response and limits its practical applications.[1] To exploit inexhaustive solar energy, it is of high interest to develop visible-light-driven photocatalysts with high performance.[2,3]

Recently, there has been much research interest in developing visible light active Bi-based photocatalysts. Bismuth oxyhalides, BiOX (X = F, Cl, Br, I), are a state-of-the-art class of photocatalysts for energy production and water purification.[4] BiOX compounds are crystallized in a tetragonal matlockite (PbFCl) structure. These compounds are identified by lamellar structures that are composed of $[Bi_2O_2]^{2+}$ slabs interleaved with double halogen atom slabs along the [001] direction.[5] Bismuth and oxygen within the $[Bi_2O_2]^{2+}$ layers are coupled through robust covalent bonding, while the interaction between $[Bi_2O_2]^{2+}$ and halogen monolayers is due to the van der Waals (vdW) force.[6] Among BiOX, bismuth oxybromide (BiOBr) has

[a] *Department of Ceramics, College of Materials Engineering, University of Babylon, 51002, Hilla, Iraq. E-mail: m.obeid8686@gmail.com*
[b] *School of Physics, The University of Sydney, New South Wales, 2006, Australia*
[c] *Department of Physics, University of Guilan, 41335-1914 Rasht, Iran*
[d] *Department of Physics, University of Antwerp, Groenenborgerlaan 171, B-2020, Antwerp, Belgium*
[e] *School of Chemistry and Chemical Engineering, Shandong University, Jinan 250100, P. R. China*
[f] *Department of Physics, College of Education for Pure Sciences, University of Babylon, Hilla, Iraq*
[g] *Department of Materials Science and Engineering, Le Quy Don Technical University, Ha Noi 100000, Vietnam*
[h] *Department of Physics, Kermanshah Branch, Islamic Azad University, P.O. Box 6718997551, Kermanshah, Iran*
[i] *Computational Optics Research Group, Advanced Institute of Materials Science, Ton Duc Thang University, Ho Chi Minh City, Vietnam*
[j] *Institute of Research and Development, Duy Tan University, Da Nang, Vietnam*
[k] *Faculty of Natural Sciences, Duy Tan University, Da Nang 550000, Vietnam*
[l] *SINTEF, Department of Materials and Nanotechnology, 0314 Oslo, Norway*
[m] *Division of Computational Physics, Institute for Computational Science, Ton Duc Thang University, Ho Chi Minh City, Vietnam*
[n] *Department of Physics, University of Oslo, P.O. Box 1048, Blindern, Oslo, Norway*

† Electronic supplementary information (ESI) available. See DOI: 10.1039/d0cp02007a

the best photocatalytic activity, but the large indirect bandgap (~2.8 eV) of BiOBr hinders its practical applications under visible light.[7] To date, a variety of BiOBr nano- and micro-structures, including microspheres, nanobelts, and nanoplates synthesized *via* various preparation methods, have been applied as photocatalysts to degrade organic contaminants.[8]

Several methods have been suggested to modulate the bandgap of BiOBr nanosheets for achieving high visible light activity, among which assembling composites and doping with other elements are two common approaches.[1,9–15] Previous experimental reports showed that metal and nonmetal doping is an excellent method to increase the photocatalytic activity of bismuth oxyhalides.[15–18] The incorporation of these dopants significantly increased the light absorption, and the separation capacity of the photogenerated carriers becomes more efficient than in bare bismuth oxyhalides. However, metallic dopants still suffer from several disadvantages, like photocorrosion of the dopants, susceptibility to the environment, and limited natural reserves.[19] Boron (B) has acted as a perfect nonmetallic candidate to be accommodated and diffused within a semiconductor crystal structure due to its intriguing physicochemical characteristics such as light weight, high chemical resistance and typical semiconductivity. Compared with other nonmetallic elements, B has a small ionic radius (0.023 nm), so it can be effortlessly merged into the crystal lattice of semiconductors. Furthermore, the electron configuration of B has one empty p-orbital and renders B electron-deficient. Thus, the chemical environment near each B atom is controlled by its electron-deficient configuration, which is anticipated to enhance charge separation in photocatalysis.[20–22] Phosphorus has an extra orbital and higher electron donating ability, so phosphorus-doped semiconductors have various positive effects such as promoting charge transfer in photocatalytic reactions.[23] From this perspective, nonmetal doping may be a more feasible approach to reduce the bandgap and improve the visible-light-driven photocatalytic performance of bismuth oxyhalides.

Previous theoretical studies using density functional theory (DFT) calculations have been performed to reveal the mechanisms behind the photocatalytic enhancement of doped bismuth oxyhalides. Zhang *et al.*[24] showed that co-doping BiOCl with Sb and I atoms could decrease the bandgap along with enhancing the optical absorption response of bulk BiOCl. Yao *et al.*[25] studied the effect of C-, N-, and S-doping on the electronic and optical properties of bulk BiOCl. The authors found that S-doped BiOCl is more stable compared to C and N doping. Furthermore, the S-doped BiOCl system has better photocatalytic activity than those of C and N doping due to the presence of impurity levels that are generated by the S atoms. These impurity levels can decrease the recombination rate of photogenerated carriers.

Nonmetal (B and P) doped BiOBr and BiOI photocatalysts were successfully prepared from $Bi(NO_3)\cdot 5H_2O$, H_3BO_3, and NaH_2PO_4 precursors using a facile synthesis route.[26,27] The incorporation of these nonmetal atoms significantly enhanced the photocatalytic performance of pristine BiOX (X = Br, I). The authors stated that it is difficult to locate the exact position of these dopants in the crystal lattice of BiOBr and BiOI. In the present work, we performed first-principles calculations to evaluate the doping sites of B and P atoms in single-layer BiOBr based on the formation energies.[28] Then, we systematically investigated the effect of these atoms on the structural, electronic, and optical properties of single-layer BiOBr photocatalysts using the CASTEP code. It is found that B doping can improve the visible light photocatalytic activity of single-layer BiOBr. This is due to the fact that the SubB-BiOBr system has a lower carrier recombination rate, higher visible light absorption edge, and more catalytically active sites. Hence, B substituted BiOBr has potential as a worthy visible light photocatalyst.

2. Computational details

First-principles calculations were achieved with the generalized gradient approximation of Perdew–Burke–Ernzerhof (GGA-PBE), as implanted in the CASTEP code.[29,30] Ultrasoft pseudopotentials were used to characterize the interaction between ion cores and valence electrons.[31] A cut-off energy of 400 eV and Monkhorst–Pack[32] *k*-point mesh of $3 \times 3 \times 1$ were adopted to perform geometry optimization and electronic structure computation. We found that a *k*-mesh of dimensions $3 \times 3 \times 1$ within the irreducible Brillouin zone (IBZ) and four empty bands were enough for converging the band structure, including the crystal local field effect *via* the random phase approximation. A finer *k*-point mesh ($9 \times 9 \times 1$) was adopted for the optical property calculation with instrumental smearing of 0.5 eV. For all atomic relaxations in this paper, the convergence criteria for the residual force and total energy were set to 3×10^{-2} eV Å^{-1} and 10^{-6} eV per atom, respectively. $3 \times 3 \times 1$ supercells were used to simulate the pristine and doped bismuth oxybromide systems.[33] A vacuum space of 15 Å was constructed along the *z*-axis to exclude the artificial interactions between neighboring slabs. The van der Waals (vdW) density functional correction method of Tkatchenko and Scheffler (TS-vdW)[34,35] was used to describe the long-range vdW interactions. The additional effect of spin–orbit coupling (SOC) was also considered during the calculation of the electronic properties due the presence of heavy elements such as bismuth.

3. Results and discussion

3.1. Geometry and structural stability

The optimized crystal structures of pristine and boron-doped BiOBr sheets are depicted in Fig. 1. The B/P–doped single-layer BiOBr structures were created by placing one boron or phosphorus atom in the $3 \times 3 \times 1$ supercell of the pristine BiOBr monolayer. Generally, there are two possible sites, substitutional and interstitial, in these oxides.[36] Since single-layer BiOBr has two Bi layers, B/P atoms may substitute Bi atoms at one or the other of these two layers. Therefore, we consider these two possible substitutional sites, SubB(P), see Fig. 1(b) and (c). For interstitial doping, IntB(P), one B(P) atom is inserted between two Bi atoms, see Fig. 1(d). Three interstitial sites have been modeled to evaluate the most stable site. The doping

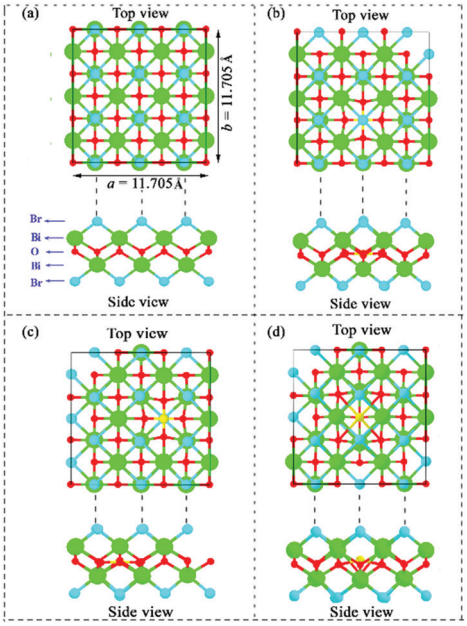

Fig. 1 Top and side views of the (001) basal plane of the optimized pristine single-layer BiOBr (a), and B-doped with the B atom substituting the first layer of Bi atoms (b) and the second layer of Bi atoms (c), and the B atom occupying the most favourable interstitial space (d). The golden spheres represents B atoms.

concentrations are 1.85% for substitutional sites and 1.81% for interstitial sites. These values are close to the experimentally determined boron and phosphorus doping concentration of BiOBr and BiOI, respectively.[26,27]

For pristine single-layer BiOBr, the calculated value of the in-plane lattice parameter using GGA-PBE + vdW is found to be 3.901 Å, which agrees well with the corresponding experimental and theoretical values 3.924 Å and 3.930 Å, respectively.[15,37] The calculated bond lengths of Bi–O and Bi–Br are 2.325 and 3.195, respectively, which are in good agreement with other DFT calculations.[38–40]

Boron (phosphorus) doping leads to a local structural distortion of single-layer BiOBr, which is characterized by the lattice constant, angle, and bond length variations, as given in Table 1. It can be seen that the lattice constant and angles of SubB-BiOBr and SubP-BiOBr sheets are reduced somewhat compared with those of the pristine single-layer BiOBr. This is attributed to the small atomic radii of the B and P atoms as compared to the Bi atom. The introduction of the dopant atoms leads to a displacement of neighboring atoms and deformation of the BiO_4 tetrahedron as well as the Br atoms that are formed with four Bi atoms in a planar square, see Fig. 1(b–d). Furthermore, significant local distortions can also be observed by the bond length variations upon doping, where the bond lengths of P–O and B–O tend to be shorter than that of Bi–O after geometry optimization, see Table 1. The results revealed that the degree of lattice distortion of phosphorus substitution is less than that of B substitution. This observation is in good agreement with a previous experimental report.[26] It is worth mentioning that both B and P atoms move off the perfect substitutional site after geometry optimization. In contrast, the lattice constant a of IntB-BiOBr and IntP-BiOBr elongates somewhat compared to that of the pristine BiOBr crystal, while other parameters remain almost constant, as seen in Table 1. The severe lattice distortion caused by B substitution may be related to the large ionic radius difference between boron (0.23 Å) and bismuth (1.03 Å).

To evaluate the most energetically favourable doping site, the defect formation energy E_f is calculated using the expressions below:[41]

$$E_{s-f} = E_{X-BiOBr} - E_{BiOBr} - \mu_X + \mu_{Bi} \quad (1)$$

$$E_{i-f} = E_{X-BiOBr} - E_{BiOBr} - \mu_X \quad (2)$$

where E_{BiOBr} and $E_{X-BiOBr}$ are the total energies of pure and doped BiOBr sheets, respectively. The symbols μ_X and μ_{Bi} are the chemical potentials of single B (or P) and Bi atoms, respectively. The chemical potentials of these atoms are calculated from the total energy of boron, phosphorus, and bismuth isolated atoms. In detail, eqn (1) and (2) are adopted to predict the formation energy of the doped structures for substituting Bi and occupation of an interstitial space, respectively. The previously reported dispersion of phonons emphasized that pristine single-layer BiOBr is dynamically stable.[37,42] However, the more negative value of E_f indicates a more stable structure.[43] The formation energies of all doped BiOBr structures were predicted under Bi-rich and O-rich conditions, see Table 2. Under the B-rich environment, $\mu_{Bi} = E(Bi)$, and $\mu_O = E_{BiOBr} - E_{Bi} - E_{Br}$. Under the O-rich environment, $\mu_O = 1/2EO_2$, and $\mu_{Bi} = E_{BiOBr} - E_O - E_{Br}$. It can be seen that all doped structures are stable, and the B-doped BiOBr structures are more stable than the P-doped systems. This may be related to the fact that boron has the smallest ionic radius (0.23 Å), so it can be easily incorporated into the crystal structure of semiconductors.[26] Interestingly, we found that the O–B–O bond tends to be flat with an angle of

Table 1 Structural parameters such as: lattice constant, bond lengths, bond angle, and average net charge of pristine and doped BiOBr sheets

			Angle (°)			Bond length (Å)			
	a (Å)	b (Å)	α	β	γ	X–O	X–Br	Bi–Br	Bi–O
BiOBr	3.901	3.901	90	90	90		—	3.195	2.325
SubB-BiOBr	3.868	3.864	90	89.99	89.99	1.595	4.086	3.150	2.300
IntB-BiOBr	3.950	3.901	90.01	89.85	90		—	3.220	3.210
SubP-BiOBr	3.871	3.871	90	90	90	1.830	3.670	3.180	3.327
IntP-BiOBr	3.974	3.915	89.81	89.12	89.12		—	3.150	2.302

Table 2 Formation energies (eV) of B/P doped single-layer BiOBr systems with various doping sites

	B		P	
Doping site	Bi-rich	O-rich	Bi-rich	O-rich
Sub (layer-1)	−5.114	−15.626	−0.974	−14.786
Sub (layer-2)	−5.114	−15.626	−0.974	−14.786
Interstitial-1	−5.186	−5.186	−2.219	−2.219
Interstitial-2	−3.216	−3.216	−1.612	−1.612

175.5°, see Fig. S1 (ESI†). The defect formation energies of both B and P doped BiOBr are negative under both Bi- and O-rich conditions but are more stable under O-rich conditions. The results indicate that doping of B and P impurities is exothermic, and the preparation of a B(P)-doped BiOBr sample should be possible and carried out under O-rich conditions. The most favourable formation energy (−15.626 eV) is obtained for B substitutional doping (SubB-BiOBr) in an O-rich environment, while it is least favourable for a substitutional site with P incorporation (SubP-BiOBr) under Bi-rich conditions. Furthermore, the calculated values are comparable or close to those of similar doped systems.[25,39,44] The O and Br substitutional sites have also been studied. The calculated formation energies show positive values of 5.145 eV and 1.482 eV for B substituted O and Br atoms, respectively, while they are 5.076 eV and 0.817 eV for P substituted O and Br, respectively. Thus, B(P) atoms are less favourable to substitute either O or Br atoms. This observation is in good agreement with the previous experimental finding.[26]

To better simulate the experimental conditions of the synthesis of non-metal doped single-layer BiOBr, four single-layer BiOBr models with 1–4 substituted B atoms were constructed. The impurity concentrations for these systems are 1.85, 3.70, 5.55, and 7.40 at%. For 3.7 at%, two B atoms are spaced far apart, while two spatial arrangements (far and near neighbouring) are used to simulate 5.55 and 7.40 at%, see Fig. S2 (ESI†). The formation energies of the doped systems are calculated as:

$$E_{s\text{–}f} = E_{X\text{–}BiOBr} - E_{BiOBr} - n\mu_X + n\mu_{Bi}/n \qquad (3)$$

where n is the number of incorporated B atoms (n = 1, 2, 3, or 4) and $E_{X\text{–}BiOBr}$ is the total energy of SubB-BiOBr. Fig. 2 displays the variation of the impurity concentrations and corresponding formation energies as a function of n. It can be seen that the formation energy of pristine BiOBr increased with increasing B content. The difference of the formation energies between two adjacent data points is 0.52–0.91 eV lower than that of single atom doped BiOBr (−15.626 eV). As a result, the preparation of pristine BiOBr and SubB-BiOBr with higher doping concentrations is achievable and controllable.

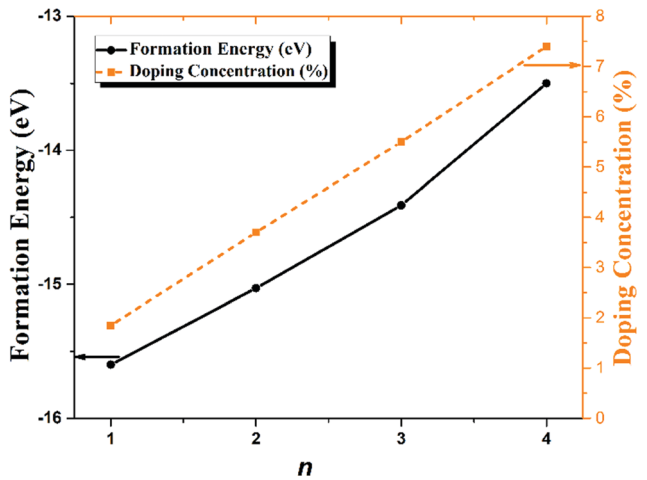

Fig. 2 Variation of the B doping concentrations and corresponding formation energies of B-doped BiOBr under O-rich conditions as a function of the number of introduced B atoms (n).

3.2. Electronic properties

In addition to the phase stability, the electronic band structure of a photocatalyst is another key property to understand its photocatalytic activity.[33] Thus, the band structures and density of states (DOS) of the pure and doped bismuth oxybromide have been calculated, as shown in Fig. 3. Based on these results, the bandgaps, locations of the valence band maximum (VBM) and conduction band minimum (CBM), and constitutions of the VB and CB are given in Table 3. The calculated bandgap of pristine single-layer BiOBr is 2.48 eV with an indirect semiconducting character. The obtained results are close to those of previously published experimental and theoretical results.[38,42,45–48] The calculated bandgap value of bulk BiOBr is 2.12 eV, which is lower by 0.35 eV than its monolayer counterpart using the GGA-PBE scheme.[40] Thus, the influence of quantum confinement on the bandgap variation from the bulk to the BiOBr single-layer configuration is not important. Fig. 3 shows the electronic band structure of single-layer BiOBr. It is seen that the valence band maximum (VBM) occurs in the region between the Γ and M special k-points of the Brillouin zones, while the VBM occurs in the region between the K and Γ points for the interstitial boron doped single-layer BiOBr. On the other hand, the conduction band minimum (CBM) always occurs at the Γ point for pristine and doped BiOBr. Thus, all these bismuth oxyhalide single-layers are mostly indirect bandgap semiconductors, as a similar trend was seen in their crystalline bulk phase band dispersion. This notable nature of the VBM dispersion has already been reported for pristine BiOBr monolayers with HSE06 level calculations.[49] Therefore, it validates the reliability of our computed values and the curves of the bands. It must be mentioned in this context that a strong overestimation of the bandgap of pristine single-layer BiOBr does not tempt us to employ the HSE06 method. For instance, the previously reported bandgap using the HSE06 functional is between 3.32 and 3.41 eV[37,42,49] against the experimental value (2.77–2.89 eV).[7,50] In other words, the HSE06 calculation overestimates the experimental bandgap by 0.52–0.55 eV, while the PBE calculation (2.48 eV) only underestimates the bandgap by 0.29–0.45 eV. Thus, our calculated bandgap using the PBE functional is reasonable. Furthermore, the applied computationally expensive HSE06 would also involve a bandgap fitting parameter without an important effect on the optical transformations. Therefore, the option of using the HSE06 method is excluded here. In the photocatalytic process, the bandgap type is essential in the recombination of photoexcited holes and electrons owing to differences in the electron decay from the CBM. A bandgap reduction is observed under the influence of spin orbit coupling, see Fig. S3 (ESI†). For semiconductors with a direct bandgap character, such as rutile TiO_2, the recombination of the charge carriers releases a photon when the VBM and CBM are positioned in an identical k-vector. On the other hand, for indirect bandgap semiconductors such as anatase, the recombination generates a phonon because

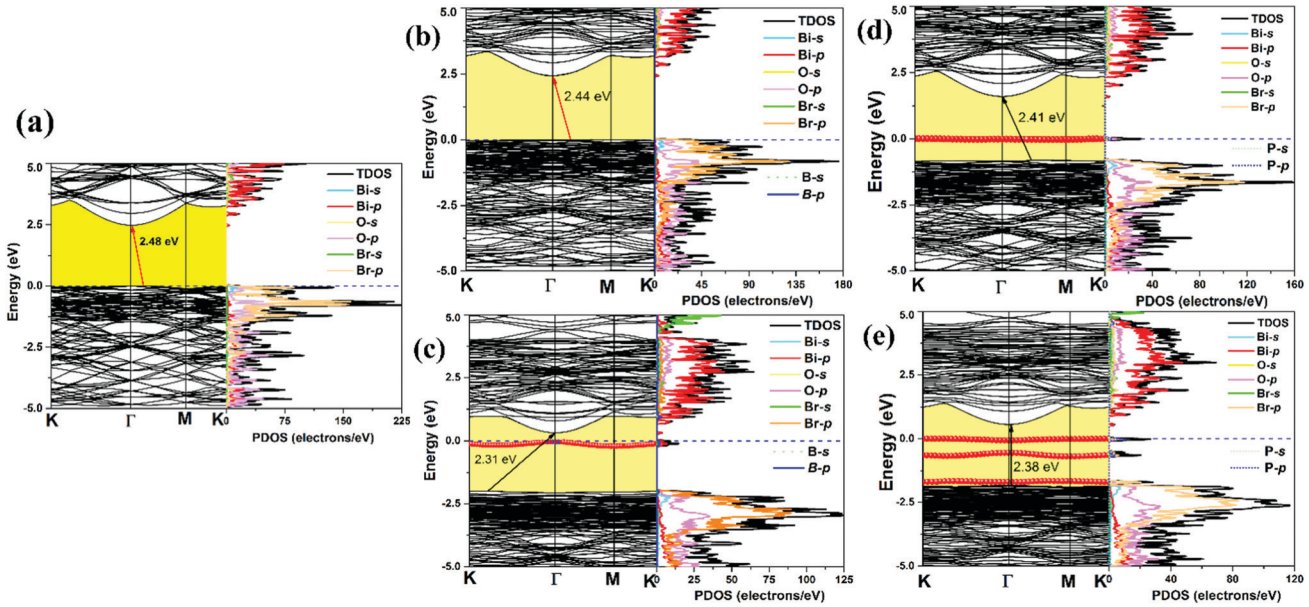

Fig. 3 Calculated band structure with the corresponding DOS and PDOS of (a) pristine BiOBr, and (b) SubB, (c) IntB, (d) SubP, and (e) IntP doped single-layer BiOBr. The horizontal dashed blue line indicates the Fermi level, which is set to zero.

Table 3 Calculated bandgaps, locations of the VBM and CBM and constituents of the VB and CB in the pristine and doped BiOBr

System	E_g (eV)	Location		Nature of the bandgap	Constituents	
		VBM	CBM		VB	CB
BiOBr	2.48	Between Γ and M	Γ	Indirect	Br, O, Bi	Bi, O
SubB-BiOBr	2.44	Between Γ and M	Γ	Indirect	Br, O, Bi, B	Bi, B, O
IntB-BiOBr	2.31	Between Γ and K	Γ	Indirect	B, Bi, Br, O	Bi, O, B
SubP-BiOBr	2.41	Between Γ and M	Γ	Indirect	P, Bi, Br, O	Bi, P, O
IntP-BiOBr	2.38	Γ	Γ	Direct	P, Br, Bi, O	Bi, O, P

of the difference between the VBM and CBM, leading to difficult recombination between excited electrons and holes, which increases the electron–hole lifetime. Consequently, the diffusion rate and the reaction time of the excited electron–hole pairs in indirect semiconductors also show an upsurge, making them favorable candidates with excellent photocatalytic activity compared to direct semiconductors.[41] Thus, the indirect bandgap BiOBr monolayer is a promising photocatalyst candidate, which advantageously decreases the occurrence of electron–hole recombination by increasing the distance in momentum space between the CBM and VBM. The partial DOS showed that the CBM of pristine BiOBr is dominated by Bi-6p states, while the VBM is mainly composed of Br-4p orbitals with clear hybridization with O-2p and Bi-6s orbitals.

The electronic band structures of different doping systems are demonstrated in Fig. 3(b–e). As presented in Fig. 3(b), the value of the bandgap of SubB-BiOBr is slightly decreased (2.44 eV) compared to that of pristine BiOBr (2.48 eV). The type of the bandgap is not changed, and the partial DOS results show a similar character to that of pristine BiOBr. In contrast, the value of the bandgap of IntB-BiOBr is noticeably reduced (2.31 eV) compared to that of the pristine structure, see Fig. 3(c). This reduction is triggered by the formation of intermediate bands (IBs) positioned above the VB. Based on the results of the PDOS, the impurity energy band (red line) is mainly attributed to a clear hybridization between B-2p and Bi-6p orbitals. Moreover, a new interstitial doping site was studied, and the electronic band structure of this new model is depicted in Fig. S4 (ESI†). The results showed that the doped system has a metallic character, where the CBM crosses the Fermi level.

The band structure of phosphorus substituted BiOBr is illustrated in Fig. 3(d). The doped system has an indirect bandgap of 2.41 eV, where the VBM is located between the Γ and M points, while the CBM is positioned at the Γ-point. It can be seen that phosphorus substitution reduced the bandgap value of pristine BiOBr more effectively than that of boron substitution. The IBs (red line) are formed due to the presence of phosphorus impurities. The IBs are composed of P-3p and O-2p orbitals. The effect of spin–orbit coupling (SOC) on the electronic band strucutre of single-layer BiOBr doped with boron (B) and phosphorus (P) atoms has also been studied, and the results showed that doped monolayer possesses an indirect bandgap structure which matches the results obtained from pure PBE functional. Indeed, the impact of SOC seems significant on the indirect bandgap for these ultrathin monolayers.

Thus, SOC effects cannot be neglected for such bismuth based compounds, see Fig. S3 (ESI†). Interestingly, the IntP-BiOBr structure has a direct bandgap character with a value of 2.38 eV, see Fig. 3(e). The partial DOS shows the formation of three occupied impurity energy bands (red lines) located in the middle of the bandgap. These impurity levels are mainly composed of P-3p and Br-4p states. Moreover, new P interstitial doping sites have also been studied. The new studied doping site shows a metallic band character, see Fig. S5 (ESI†). In the IntB-BiOBr structure, the IBs (B-2p and Bi-6p states) are close to the CBM. Hence, it becomes an n-type semiconductor, as the interstitial doping atoms introduce additional electrons into the system. The most stable doped systems have an indirect bandgap structure, which is beneficial in photocatalytic practice. As presented in Fig. 3, B and P dopants are able to modify the electronic band structure of the pristine BiOBr monolayer, such as the number and shape of the IBs (dispersed or flat), and the energy positions of the VBM and CBM and constituents of the CB and VB. These results are also tabulated in Tables 3 and 5. Therefore, they can tune the photocatalytic activity of the pristine BiOBr monolayer.

Indeed, there are four fundamental factors, namely an appropriate bandgap value, a low e^-/h+ recombination rate, rich catalytically active sites, and a proper work function, which are related to the photocatalytic ability of common semiconductors.[51] BiOBr-based catalysts have intrinsically outstanding optical absorption properties. As a result, we have to study all of these factors and more details will be deliberated in the next subsections.

To gain further insight into the chemical bonding properties of pure and doped BiOBr sheets, Mulliken population analyses have been conducted to determine the average net charge and bond population values, which are recorded in Table 4. Furthermore, the electron density distribution and electron density difference ($\Delta\rho$) of the pristine and doped single-layer BiOBr systems are depicted in Fig. S6 and S7 (ESI†), respectively. The electron density difference is defined as $\Delta\rho = \rho_{Tot} - \rho_{Pristine} - \rho_{Dopant}$, in which ρ_{Tot}, $\rho_{Pristine}$ and ρ_{Dopant} represent the electron density of the doped system, the monolayers, and the isolated dopants, respectively. For pristine single-layer BiOBr, the chemical bonding between Bi and O atoms mainly shows the feature of a covalent bond. This is due to the large electronegativity difference between O (3.44) and Bi (2.02) atoms. This is also clear from the non-spherical shape of the electron density around O and Bi atoms, see Fig. S6(a) (ESI†). The electron density difference exhibits closely how the electron density varies during the doping process. The charge density distribution of pristine and doped single-layer BiOBr is plotted in Fig. S6 (ESI†). Blue denotes a loss of electrons, while red symbolizes electron enrichment. In Fig. S7(a) (ESI†), the small overlap among the neighboring electron clouds between the Bi and O atoms in the defect-free single-layer BiOBr demonstrates the presence of covalent Bi–O bonding. The covalent bonding character of pristine BiOBr is confirmed by the positive values of the bond population, see Table 4. The results are in line with other theoretical findings.[38,52] For SubB(P)-BiOBr models, the bond length between B(P) and O atoms became shorter than that of Bi–O, see Fig. S7(b)–(d) (ESI†). The electron density of the B(P)–O bond extends visibly from the B(P) atom to the O atom, which indicates that the B(P)–O bond strengths are stronger than that of the Bi–O bond. The electron density around interstitial dopants is less than that around substitutional ones, as shown in Fig. S7(c)–(e) (ESI†). Furthermore, the population values of the doped models become larger (Table 4), and the bond lengths become shorter (Table 1), indicating that the O–X bonds, especially for substitution structures, are stronger than those of the undoped system and present a strong covalent property. Compared with pristine BiOBr, the variation of the average net charge of atoms that neighbor the B(P) impurity is more obvious, while the variation of the average net charge of atoms that are far away from the B(P) impurity is negligible. According to the charge transfer listed in Table 4, Q of the B and P dopants is positive, which proposes that the doped structures are n-type semiconductors.

3.3. Effective mass of photoexcited carriers

The separation and diffuse rate of the photogenerated electrons and holes are key factors for an outstanding photocatalyst.[53] Generally, for a photocatalyst with lighter effective mass, its carriers will have more probability of reaching the surface reaction sites, thus improving the photocatalytic activity. As well, a superior difference between the effective masses of the electrons and holes will decrease their recombination rate. The transfer rate of the photoexcited electrons and holes can be predicted by their effective masses, which can be explained by the formula, $\nu = \hbar k/m^*$, where k is the wave vector, $\hbar$ is the reduced Planck constant, and m^* is the effective mass of the carriers.[54] Regularly, the transfer rate is inversely proportional to the effective masses of electrons and holes, where lighter charge carriers will transfer faster. The effective masses of the electrons (m_e^*), and holes (m_h^*) are calculated by fitting the

Table 4 The calculated average net charge and bond population values of pristine and doped BiOBr using Mulliken population analysis

	Average net charge/e (Q)				Population/e							
System	X	Bi	O	Br	O_1–Bi	O_1–X	O_2–Bi	O_2–X	O_3–Bi	O_3–X	O_4–Bi	O_4–X
BiOBr		1.40	−0.91	−0.50	0.19		0.19		0.19		0.19	
SubB-BiOBr	0.79	1.39	−0.86	−0.49		0.55		0.55		0.54		0.54
IntB-BiOBr	0.05	1.35	−0.84	−0.49		0.96		−0.04		−0.05		−0.05
SubP-BiOBr	1.20	1.40	−0.9	−0.49		0.23		0.23		0.23		0.23
IntP-BiOBr	0.40	1.35	−0.9	−0.49		0.22		−0.06		−0.07		−0.07

Table 5 Calculated results of the pristine and doped BiOBr. m_e*, m_{IBs}* and m_h* are the effective masses of the CB, IBs and VB compared with m_0, respectively. R = m_h*/m_e* or m_e*/m_h* is defined as the relative effective mass. N is the number of catalytically active sites

System	BiOBr	SubB-BiOBr	IntB-BiOBr	SubP-BiOBr	IntP-BiOBr
m_e*	0.34	0.33	0.30	0.32	0.36
m_{IBs}*			0.77	7.48	7.16
					1.20
					7.18
m_h*	2.59	3.94	1.84	2.15	3.33
R	7.61	11.93	6.13	6.71	9.25

parabolic shape of the CBM and VBM of pristine and doped BiOBr monolayers, respectively, utilizing eqn (4):[55]

$$m^* = \hbar^2/(d^2E/dk^2) \quad (4)$$

where E is the energy of an electron at a wave vector k in the CBM and VBM. The estimated values are tabulated in Table 5. The latter shows that m_e* is nearly one order of magnitude lower than m_h* for all samples, indicating easier migration of photogenerated electrons to the reaction site in the photocatalytic process. Larger m_h* leads to slow diffusion of the photoexcited holes. The calculated values of m_e* and m_h* for the pristine BiOBr monolayer are close to the values obtained by Zhang *et al.*[37] and Sun *et al.*[42] using the HSE06 functional. Interestingly, compared with the defect-free BiOBr monolayer, the photoinduced electrons and holes in B substituted BiOBr become lighter and heavier, respectively. This observation in the SubB-BiOBr structure is valuable for the separation of photoexcited electron and holes, and further enhances its photocatalytic performance. We also find that there are large differences between m_e* and m_h*. This large difference results in anisotropic transfer mobility and slower recombination rates of the electron–hole pairs. Thus, they have different diffusion lengths ($L_P = (\mu k_b \tau/e)^{1/2} = (\mu k_b \tau^2/m^*)^{1/2}$). The larger the difference of L_P, the lower the recombination rate.[56] To numerically predict the impact of the doping strategy on the recombination rate, the relative mass (R) of electron–hole pairs of the pristine and doped samples must be calculated using $R = m_h^*/m_e^*$.[51] A larger R value indicates a larger difference in L_P, resulting in a low recombination rate and higher photocatalytic activity. The calculated values of R are tabulated in Table 5.

The results revealed that the SubB-BiOBr system has the largest R value as compared to other structures, suggesting that B substitution can lead to a slower recombination rate of electrons and holes, and boosts the photocatalytic performance of single-layer BiOBr.

3.4. Photocatalytic performance

Catalytically active sites were studied *via* the calculations of the highest occupied molecular orbitals (HOMO) and lowest unoccupied molecular orbitals (LUMO). As presented in Fig. 4(a), the HOMO covers most of the O atoms and a few Br atoms while the LUMO is mainly distributed on the first and second layers of Bi atoms. This reflection is in good agreement with the PDOS spectra. It is important to note that pristine BiOBr has few catalytically

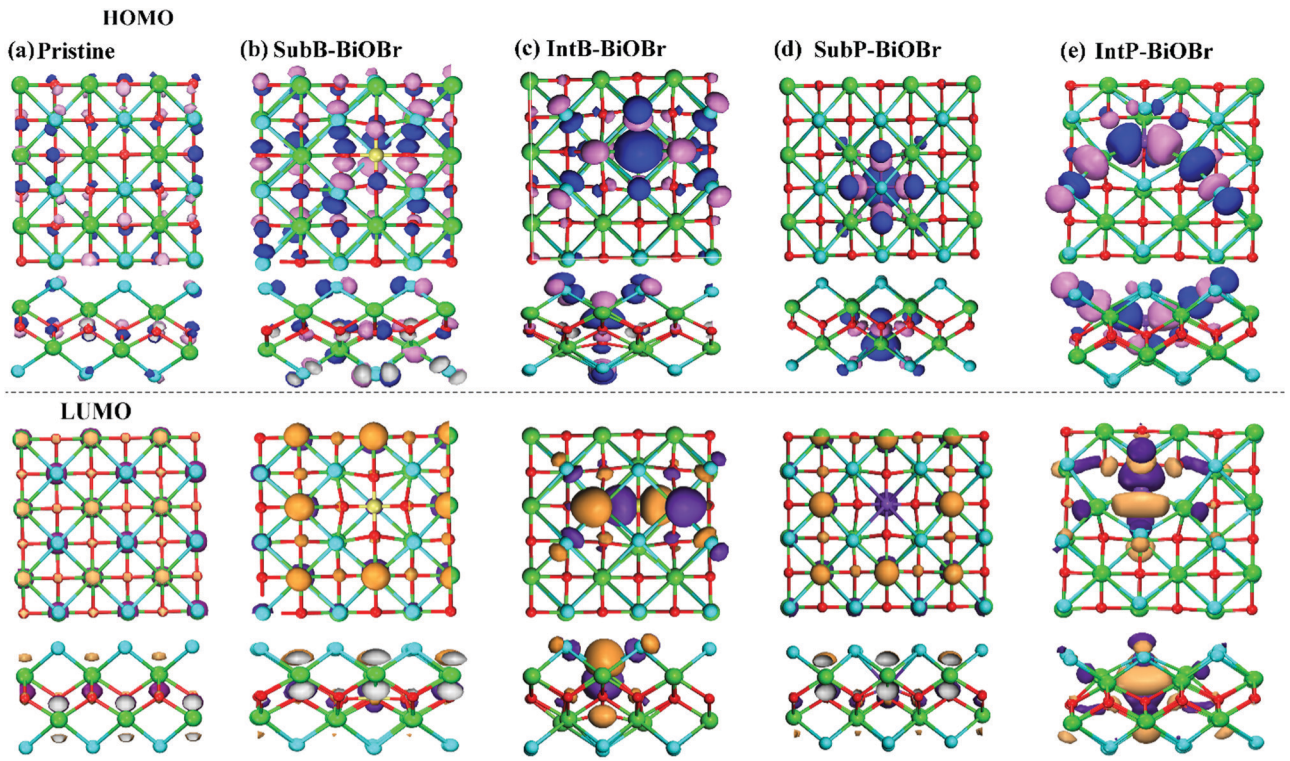

Fig. 4 Calculated HOMO and LUMO of (a) pristine BiOBr, and (b) SubB, (c) IntB, (d) SubP, and (e) IntP doped single-layer BiOBr. The isovalue is set as 0.03 electron per Å.

active sites, especially at its surface (Br atoms). Thus, the photo-induced electrons and holes might recombine again after being excited, which leads to poor photocatalytic performance.

The calculated HOMO and LUMO of the B substituted BiOBr monolayer are depicted in Fig. 4(b). In comparison with the HOMO of defect-free BiOBr in Fig. 4(a), it can be seen that the number of active sites has been increased significantly, and the two lobes of the p-orbital are localized especially on Br atoms, which leads to more active BiOBr sites at the surface. Thus, the introduction of B atoms tends to increase the carrier mobility with efficient separation of photogenerated e^-/h^+ pairs. Similar to the LUMO of pristine BiOBr, the LUMO of the SubB-BiOBr structure is distributed on the Bi atoms. For the IntB-BiOBr, SubP-BiOBr, and IntP-BiOBr doped structures, the lobes of HOMO–LUMO get bigger with fewer numbers of active sites as compared to that of SubB-BiOBr system, see Fig. 4(c–e). It can be seen that the HOMOs are localized around the dopants, indicating that electrons move from B/P atoms towards O and Br atoms. These results are in line with the PDOS examination.

The band edge potentials of the valence band (VB) and conduction band (CB) of the pristine and doped BiOBr monolayer with reference to the absolute vacuum scale are depicted in Fig. 5. The procedure of calculating the bandgap alignment can be found in detail elsewhere.[57,58] The redox potential relies on the pH value. The typical reduction and oxidation potentials for H^+/H_2 and O_2/H_2O were calculated using the following equations:[59]

$$E^{red}_{H^+/H_2} = -4.44\ \text{eV} + \text{pH} \times 0.059\ \text{eV} \quad (5)$$

$$E^{ox}_{O_2/H_2O} = -5.67\ \text{eV} + \text{pH} \times 0.059\ \text{eV} \quad (6)$$

BiOX is unstable in an acidic environment and can react with S_2 to transform to Bi_2S_3.[60] Thus, the redox potential for the water splitting reaction at pH = 7 was also predicted. At pH = 0, the CBM of the pristine BiOBr monolayer is lower (by ~0.48 eV) than the reduction potential of H^+/H_2 (positioned at −4.44 eV), while its VBM is more positive (by ~1.74 eV) than the oxidation potential of O_2/H_2O (positioned at 5.67 eV), see Fig. 5. The predicted valence band edge position is in acceptable agreement with previously published theoretical and experimental results.[37,61] The result indicates that the pristine BiOBr monolayer has a robust oxidation ability, but it failed to reduce H^+ to H_2. This statement is in line with earlier experimental and theoretical reports.[38,62]

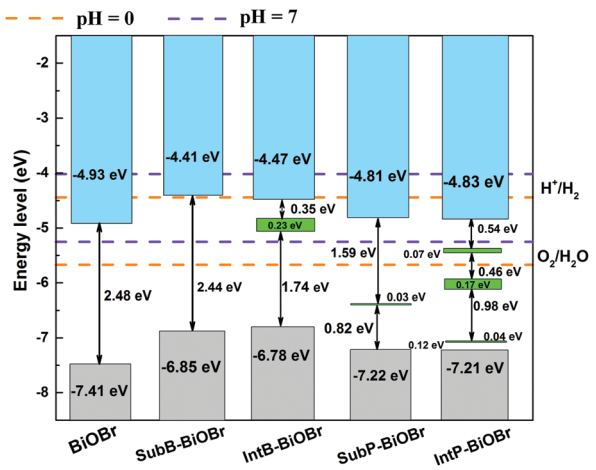

Fig. 5 The band edge position of the pristine and doped BiOBr sheets with respect to the water reduction and oxidation potentials at pH = 0 and pH = 7. The blue and gray regions stand for the CBM and VBM, while the intermediate bands (bandwidth) are labeled with green lines.

For the SubB-BiOBr structure, the CBM and VBM both shift upward with respect to the bare BiOBr monolayer by 0.52 and 0.56 eV, respectively. The upward shifting of the CBM and VBM indicates that the SubB-BiOBr structure has a strong reduction/oxidation ability, and can effectively harvest solar light. Thus, bismuth oxybromide substituted with boron can be considered as a potential candidate for overall water splitting. This observation is in good agreement with the experimental finding.[26] In the case of B interstitial doping, the CBM becomes more negative as compared to the pristine BiOBr monolayer and has a good reduction ability. Furthermore, the VBM moves upward by ~0.68 eV, and hence the driving force for water photo-oxidation is reduced. Also, B interstitial doping leads to occupied and localized intermediate bands (IBs) within the bandgap. The IBs are beneficial for the transfer of photogenerated carriers to reactive sites at the catalyst surface.[38] In the SubP-BiOBr system, the VBM and CBM positions have been improved compared to the pristine BiOBr monolayer. A similar trend has been found in the experiment.[27] Furthermore, the H^+/H^2 potential is located above the CBM, while the O_2/H_2O potentials are positioned above the VBM and IBs. This indicates the strong oxidizing abilities of the doped system. The band edges of the studied structures have a strong oxidation ability of water even in a neutral environment (pH = 7). Among all the studied models, BiOBr with B substitution is a promising candidate for photo-electrochemical water splitting since it has an appropriate bandgap (2.44 eV), many catalytically active sites, a high carrier mobility, a low recombination rate and a good band edge alignment with the water reduction and oxidation potentials.

The work function (Φ) is decisive for determining the photocatalytic activity of 2D materials, as the work function shows the ability of electrons to escape from the surface and react with molecules.[63] The work function is defined as the minimum energy needed for an electron to move from the Fermi level into a vacuum. Based on this definition, Φ of pristine and doped single-layer BiOBr was calculated using the formula $\Phi = E_{vac} - E_F$, where E_{vac} and E_F are the vacuum level and Fermi level, respectively. Fig. 6 shows the calculated work functions of pristine and doped BiOBr sheets. The calculated work function of defect-free BiOBr is 6.95 eV, see Fig. 6(a). It is well known that BiOBr is a p-type semiconductor.[42] Upon doping, the Fermi level may move into the valence/conduction band region, together with the increase/decrease of the work functions, thus leading to p-/n-type doping of BiOBr.[64] The introduction of interstitial B(P) atoms induces a reduction in the work function of the pristine BiOBr sheet, see Fig. 6. Such an observation indicates that the single-layer BiOBr is tuned into an n-type material by doping with B atoms, and it is

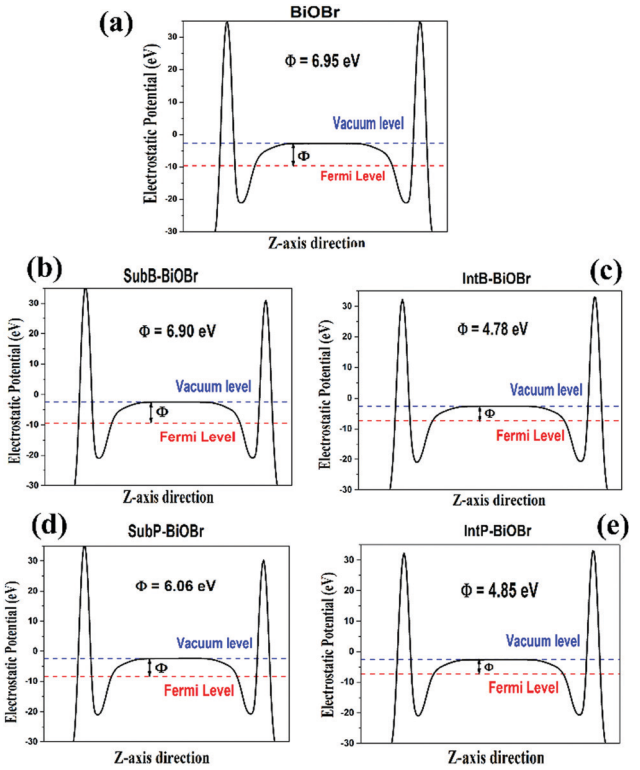

Fig. 6 Work function of pristine (a) and B (b and c) and P (d and e) doped single-layer BiOBr. The blue and red dash lines are the vacuum and Fermi levels, respectively.

consistent with the band structure results. The observed reduction in the work functions of the doped models is beneficial for enhancing the photocatalysis performance.

3.5. Optical properties

All the computations of the optical properties have been performed using density functional theory (DFT) containing the dispersion-correction at the TS level. The optical properties of pristine and doped single-layer BiOBr systems are discussed on the basis of the imaginary part of the dielectric function ($\varepsilon(\omega)$) and absorption spectra, as displayed in Fig. 7, where ω is the incident photon frequency. The dielectric function is known as $\varepsilon(\omega) = \varepsilon_1(\omega) + i\varepsilon_2(\omega)$, where ε_1 and ε_2 are the real and imaginary parts of the dielectric function. ε_2 is an operative parameter to quantify the optical absorption capability of solids. In Fig. 7(a), one can see that the interstitial doping has a significant impact on the optical spectrum of the defect-free system. For the pristine BiOBr monolayer, the optical absorption edge starts at ~495 nm (2.50 eV), which is close to the value of the calculated indirect bandgap. For B(P) substitutional models, the optical absorption edges are slightly shifted to lower energy levels (*i.e.* a red-shift). A significant red-shift can be seen for the interstitially doped structures. This observation is consistent with the bandgap reduction.

The optical absorption coefficient $\alpha(\omega)$ is obtained from the dielectric components using the following formula:[65,66]

$$\alpha(\omega) = \sqrt{2\omega}\left[\sqrt{\varepsilon_1(\omega)^2 + \varepsilon_2(\omega)^2} - \varepsilon_1(\omega)\right]^{1/2} \quad (7)$$

The optical absorption spectra of pristine and doped BiOBr are depicted in Fig. 7(b). It can be seen that nonmetal doped BiOBr structures show a clear red-shift and the optical absorption edges are enhanced as well. The results are in line with previous experimental reports.[26,27] The absorption intensity of the substitutional dopants is overlapped with that of pristine BiOBr, while a significant absorption intensity reduction is observed for the interstitial doping.

4. Conclusions

In the present work, the electronic band structures and optical properties of pristine and nonmetal doped BiOBr sheets have been studied based on first-principles calculations. Due to its

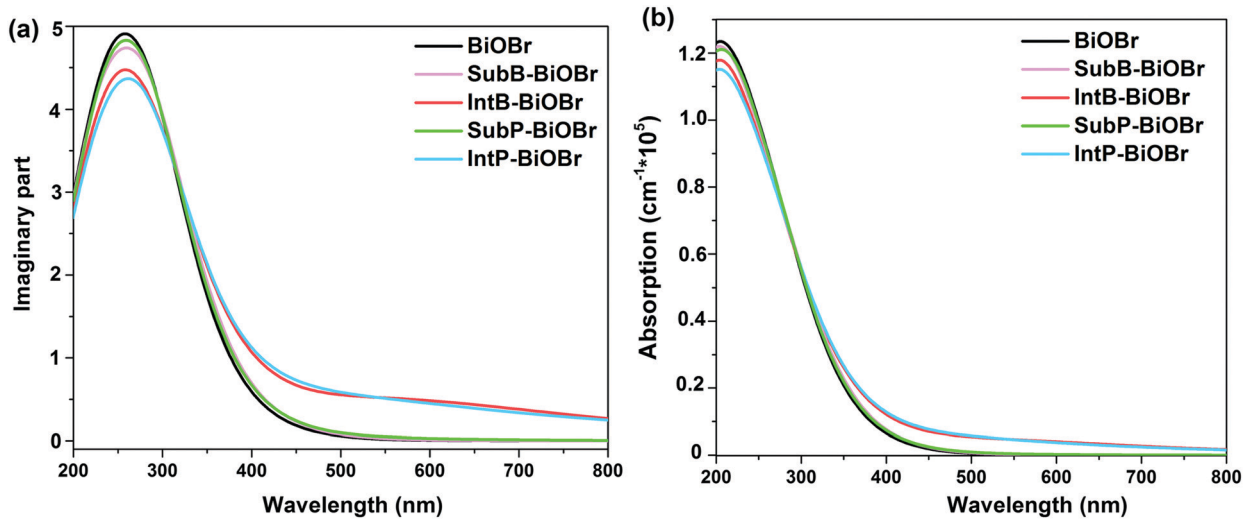

Fig. 7 Optical properties *i.e.* the (a) dielectric constant and (b) optical absorption of pristine and doped single-layer BiOBr.

small ionic radius, boron (B) can be easily merged into the crystal lattice of semiconductors. Furthermore, the electron configuration of B has one empty p-orbital and renders B electron-deficient, which is anticipated to enhance charge separation in photocatalysis. Phosphorus (P) has an extra orbital and higher electron donating ability, so P-doped semiconductors are predicted to promote charge transfer in photocatalytic reactions. Severe lattice distortions occur, which may be related to the large ionic differences between B(P) and Bi atoms. The pristine single-layer BiOBr is a semiconductor with an indirect bandgap of 2.48 eV. The nature of the indirect bandgap of pristine BiOBr remains for SubB-BiOBr, SubP-BiOBr, and IntP-BiOBr models with values of 2.44 eV, 2.42 eV, and 2.22 eV, respectively. In contrast, B interstitial doping may cause an indirect-to-direct bandgap transition. The conduction band bottom of B substituted BiOBr becomes more negative compared to the other structures, indicating that B substituted BiOBr sheets have a stronger reducing activity. Additionally, B-doped BiOBr has shown exceptional photocatalytic activity since it can suppress the recombination of photogenerated e^-/h^+, shows redistribution of the HOMO and LUMO, and can increase the number of photocatalytically actives active sites. Also, the nonmetal-doped BiOBr structures show enhanced optical absorption responses and reduced work functions. It should be noted that an appropriate doping strategy should be used to achieve suitable photoelectrochemical properties. The present results offer fruitful guidelines for designing novel nonmetal-doped BiOBr photocatalysts.

Conflicts of interest

There are no conflicts to declare.

Acknowledgements

This work was partially supported by the financial support from the Natural Science Foundation of China (Grant No. 11904203) and the Fundamental Research Funds of Shandong University (Grant No. 2019GN065).

References

1 H. Lin, X. Li, J. Cao, S. Chen and Y. Chen, *Catal. Commun.*, 2014, **49**, 87–91.
2 H. Cheng, B. Huang and Y. Dai, *Nanoscale*, 2014, **6**, 2009–2026.
3 H. T. Nguyen, T. V. Vu, N. T. Binh, D. Hoat, N. V. Hieu, N. T. Anh, C. V. Nguyen, H. V. Phuc, H. R. Jappor and M. M. Obeid, *Chem. Phys.*, 2019, **529**, 110543.
4 L. Ye, J. Liu, Z. Jiang, T. Peng and L. Zan, *Appl. Catal., B*, 2013, **142**, 1–7.
5 Q. Wang, Z. Liu, D. Liu, G. Liu, M. Yang, F. Cui and W. Wang, *Appl. Catal., B*, 2018, **236**, 222–232.
6 J. Li, H. Li, G. Zhan and L. Zhang, *Acc. Chem. Res.*, 2017, **50**, 112–121.
7 L. Lu, M.-y. Zhou, L. Yin, G.-w. Zhou, T. Jiang, X.-k. Wan and H.-x. Shi, *J. Mol. Catal. A: Chem.*, 2016, **423**, 379–385.
8 G. Jiang, X. Li, Z. Wei, T. Jiang, X. Du and W. Chen, *Powder Technol.*, 2014, **260**, 84–89.
9 X. Jia, J. Cao, H. Lin, M. Zhang, X. Guo and S. Chen, *Appl. Catal., B*, 2017, **204**, 505–514.
10 Z.-Y. Zhao, Q.-L. Liu and W.-W. Dai, *Sci. Rep.*, 2016, **6**, 31449.
11 M. Li, H. Huang, S. Yu, N. Tian, F. Dong, X. Du and Y. Zhang, *Appl. Surf. Sci.*, 2016, **386**, 285–295.
12 J. Guo, X. Liao, M.-H. Lee, G. Hyett, C.-C. Huang, D. W. Hewak, S. Mailis, W. Zhou and Z. Jiang, *Appl. Catal., B*, 2019, **243**, 502–512.
13 M. M. Obeid, *Appl. Surf. Sci.*, 2020, **508**, 144824.
14 M. M. Obeid, H. R. Jappor, K. Al-Marzoki, I. A. Al-Hydary, S. J. Edrees and M. M. Shukur, *RSC Adv.*, 2019, **9**, 33207–33221.
15 X. C. Song, Y. F. Zheng, H. Y. Yin, J. N. Liu and X. D. Ruan, *New J. Chem.*, 2016, **40**, 130–135.
16 Z. Liu, B. Wu, Y. Zhao, J. Niu and Y. Zhu, *Ceram. Int.*, 2014, **40**, 5597–5603.
17 J. Yu, B. Wei, L. Zhu, H. Gao, W. Sun and L. Xu, *Appl. Surf. Sci.*, 2013, **284**, 497–502.
18 Y. Zhang, M. Park, H. Y. Kim, B. Ding and S.-J. Park, *Sci. Rep.*, 2017, **7**, 1–12.
19 M. Sathish, B. Viswanathan and R. Viswanath, *Appl. Catal., B*, 2007, **74**, 307–312.
20 N. Lu, X. Quan, J. Li, S. Chen, H. Yu and G. Chen, *J. Phys. Chem. C*, 2007, **111**, 11836–11842.
21 A. Bafekry, S. Farjami Shayesteh and F. M. Peeters, *J. Phys. Chem. C*, 2019, **123**, 12485–12499.
22 A. Bafekry, C. Stampfl, B. Akgenc and M. Ghergherehchi, *Phys. Chem. Chem. Phys.*, 2020, **22**, 2249–2261.
23 J. Yu, Q. Li, S. Liu and M. Jaroniec, *Chem. – Eur. J.*, 2013, **19**, 2433–2441.
24 L. Zhang, Z.-K. Tang, W.-M. Lau, W.-J. Yin, S.-X. Hu and L.-M. Liu, *Phys. Chem. Chem. Phys.*, 2017, **19**, 20968–20973.
25 Y. Wen-Zhi, Y. Jian-Bin, Z. Xia and M. Ya-Hao, *Chin. J. Struct. Chem.*, 2019, **38**, 509–523.
26 D. Wu, S. Yue, W. Wang, T. An, G. Li, H. Y. Yip, H. Zhao and P. K. Wong, *Appl. Catal., B*, 2016, **192**, 35–45.
27 F.-Q. Ma, J.-W. Yao, Y.-F. Zhang and Y. Wei, *RSC Adv.*, 2017, **7**, 36288–36296.
28 P. Zhou, J. Yu and Y. Wang, *Appl. Catal., B*, 2013, **142**, 45–53.
29 S. J. Clark, M. D. Segall, C. J. Pickard, P. J. Hasnip, M. I. Probert, K. Refson and M. C. Payne, Zeitschrift für Kristallographie-Crystalline, *Materials*, 2005, **220**, 567–570.
30 M. M. Obeid, S. J. Edrees and M. M. Shukur, *Superlattices Microstruct.*, 2018, **122**, 124–139.
31 G. Kresse and D. Joubert, *Phys. Rev. B: Condens. Matter Mater. Phys.*, 1999, **59**, 1758.
32 H. J. Monkhorst and J. D. Pack, *Phys. Rev. B: Condens. Matter Mater. Phys.*, 1976, **13**, 5188.
33 H. Zhang, L. Liu and Z. Zhou, *RSC Adv.*, 2012, **2**, 9224–9229.
34 A. Tkatchenko and M. Scheffler, *Phys. Rev. Lett.*, 2009, **102**, 073005.

35 H. R. Jappor, M. M. Obeid, T. V. Vu, D. Hoat, H. D. Bui, N. N. Hieu, S. J. Edrees, Y. Mogulkoc and R. Khenata, *Superlattices Microstruct.*, 2019, **130**, 545–553.
36 M. Li, J. Li, C. Guo and L. Zhang, *Chem. Phys. Lett.*, 2018, **705**, 31–37.
37 X. Zhang, B. Li, J. Wang, Y. Yuan, Q. Zhang, Z. Gao, L.-M. Liu and L. Chen, *Phys. Chem. Chem. Phys.*, 2014, **16**, 25854–25861.
38 Z.-Y. Zhao and W.-W. Dai, *Inorg. Chem.*, 2014, **53**, 13001–13011.
39 S. Zhou, T. Shi, Z. Chen, D. S. Kilin, L. Shui, M. Jin, Z. Yi, M. Yuan, N. Li and X. Yang, *Catalysts*, 2019, **9**, 198.
40 S. Dutta, T. Das and S. Datta, *Phys. Chem. Chem. Phys.*, 2018, **20**, 103–111.
41 B. Zhu, J. Zhang, C. Jiang, B. Cheng and J. Yu, *Appl. Catal., B*, 2017, **207**, 27–34.
42 J. Yu, T. Li and Q. Sun, *J. Appl. Phys.*, 2019, **125**, 205111.
43 M. M. Obeid, H. R. Jappor, K. Al-Marzoki, D. Hoat, T. V. Vu, S. J. Edrees, Z. M. Yaseen and M. M. Shukur, *Comput. Mater. Sci.*, 2019, **170**, 109201.
44 W. Yang, Y. Wen, R. Chen, D. Zeng and B. Shan, *Phys. Chem. Chem. Phys.*, 2014, **16**, 21349–21355.
45 D. Wu, L. Ye, H. Y. Yip and P. K. Wong, *Catal. Sci. Technol.*, 2017, **7**, 265–271.
46 H. Feng, Z. Xu, L. Wang, Y. Yu, D. Mitchell, D. Cui, X. Xu, J. Shi, T. Sannomiya and Y. Du, *ACS Appl. Mater. Interfaces*, 2015, **7**, 27592–27596.
47 H. Yu, H. Huang, K. Xu, W. Hao, Y. Guo, S. Wang, X. Shen, S. Pan and Y. Zhang, *ACS Sustainable Chem. Eng.*, 2017, **5**, 10499–10508.
48 J. Chen, M. Guan, W. Cai, J. Guo, C. Xiao and G. Zhang, *Phys. Chem. Chem. Phys.*, 2014, **16**, 20909–20914.
49 M. Barhoumi, A. Abboud, L. Debbichi, M. Said, T. Björkman, D. Rocca and S. Lebègue, *Beilstein J. Nanotechnol.*, 2019, **10**, 823–832.
50 J. Wu, X. Li, W. Shi, P. Ling, Y. Sun, X. Jiao, S. Gao, L. Liang, J. Xu and W. Yan, *Angew. Chem.*, 2018, **130**, 8855–8859.
51 Y. Zhao, J. Tu, Y. Sun, X. Hu, J. Ning, W. Wang, F. Wang, Y. Xu and L. He, *J. Phys. Chem. C*, 2018, **122**, 26570–26575.
52 T. Li, X. Zhang, C. Zhang, R. Li, J. Liu, R. Lv, H. Zhang, P. Han, C. Fan and Z. Zheng, *Phys. Chem. Chem. Phys.*, 2019, **21**, 868–875.
53 K. Takanabe, *ACS Catal.*, 2017, **7**, 8006–8022.
54 W. Yu, J. Zhang and T. Peng, *Appl. Catal., B*, 2016, **181**, 220–227.
55 J. Yu, P. Zhou and Q. Li, *Phys. Chem. Chem. Phys.*, 2013, **15**, 12040–12047.
56 Y. Zhao, J. Tu, Y. Zhang, X. Hu, Y. Xu and L. He, *J. Catal.*, 2020, **382**, 280–285.
57 Y. Zhao, Y. Lin, G. Wang, Z. Jiang, R. Zhang and C. Zhu, *Appl. Surf. Sci.*, 2019, **463**, 809–819.
58 M. Mousavi, A. Habibi-Yangjeh and M. Abitorabi, *J. Colloid Interface Sci.*, 2016, **480**, 218–231.
59 X. Zhang, X. Zhao, D. Wu, Y. Jing and Z. Zhou, *Adv. Sci.*, 2016, **3**, 1600062.
60 B. Pare, B. Sarwan and S. Jonnalagadda, *J. Mol. Struct.*, 2012, **1007**, 196–202.
61 B. Yang, W. Bi, Y. Wan, X. Li, M. Huang, R. Yuan, H. Ju, W. Chu, X. Wu and L. He, *Sci. China: Chem.*, 2018, **61**, 1572–1580.
62 H.-Y. Xu, X. Han, Q. Tan, X.-L. He and S.-Y. Qi, *Catalysts*, 2017, **7**, 153.
63 W. Zhang, G. Zhu, W. Yang, Q. Sun, Q. Wu, Y. Tian, Z. Zhang, S. Zhang, S. Cheng and C. Zhang, *J. Theor. Comput. Chem.*, 2018, **17**, 1850031.
64 F. Yang, F. Xia, J. Hu, C. Zheng, J. Sun and H. Yi, *RSC Adv.*, 2018, **8**, 1899–1904.
65 M. M. Obeid, M. M. Shukur, S. J. Edrees, R. Khenata, M. Ghebouli, S. A. Khandy, A. Bouhemadou and H. R. Jappor, *Chem. Phys.*, 2019, **526**, 110414.
66 L. Azzouz, M. Halit, M. Rérat, R. Khenata, A. Singh, M. Obeid, H. Jappor and X. Wang, *J. Solid State Chem.*, 2019, **279**, 120954.

